applied sciences

MDPI

Article

Stability of a Compacted Sand Slope Model Subject to Crest Load

Said Djelabi [1], Hatem Karoui [2], Wissem Frikha [2], Mahmoud Dlala [1], Mounir Bouassida [2,*], Tarek Ninouh [3] and Moufida El May [1]

[1] Laboratoire des Risques Dangereux et Naturels, Faculté des Sciences de Tunis, Université de Tunis El Manar, Foyer Universitaire, 20 Rue de Tolède, Tunis 2092, Tunisia; said.djelabi@fst.utm.tn (S.D.); moufida.elmay@fst.utm.tn (M.E.M.)
[2] Laboratoire d'Ingénierie Géotechnique et de Géorisque LR14ES03, Ecole Nationale d'Ingénieurs de Tunis, Université de Tunis El Manar, BP 37 Le Belvédère, Tunis 1002, Tunisia; hatem.karoui@enit.utm.tn (H.K.); wissem.frikha@enit.utm.tn (W.F.)
[3] Faculté de Génie Civil, Université de Larbi Tebessi, Route de Constantine, Tebessa 12022, Algeria; tarek.ninouh@univ-tebessa.dz
* Correspondence: mounir.bouassida@enit.utm.tn

Abstract: Studying the stability of slopes is of great interest since it is associated to various geotechnical applications, e.g., access embankments and landslide mitigation. This paper describes the research conducted to determine the failure load applied at the top of excavations in sandy soils during the construction of deep digs without the use of retaining systems. An experimental program was performed to measure the failure load of ten laboratory-compacted sand slope models that were constructed using different slope angle values and different locations for the applied loading, which consisted of an imposed uniform rate of vertical displacement at the top of the slope. Then, a three-dimensional (3D) numerical model of the laboratory tests was developed to simulate the observed behavior during the experiments by the Plaxis 3D code. The Mohr–Coulomb (MC) and hardening soil (HS) models were used to describe the behavior of the compacted sand. The results showed that the 3D numerical simulations based on the MC model were able to predict the measured failure load within a relative difference of less than 11% for nine tested slope models, while the HS model was better in predicting the measured failure load (a relative difference of 3.5%) for only one experimental setup when the slope angle was equal to 35°. Furthermore, analytical prediction of the failure load using the yield design theory (YDT) permitted the validation of the log-spiral curve describing the observed failure surface for the tested sand slope models.

Keywords: behavior; failure load; rigid foundation; sand; slope

Citation: Djelabi, S.; Karoui, H.; Frikha, W.; Dlala, M.; Bouassida, M.; Ninouh, T.; El May, M. Stability of a Compacted Sand Slope Model Subject to Crest Load. *Appl. Sci.* **2023**, *13*, 5562. https://doi.org/10.3390/app13095562

Academic Editor: Cheng-Yu Ku

Received: 17 February 2023
Revised: 13 April 2023
Accepted: 14 April 2023
Published: 29 April 2023

1. Introduction

The behavior of human-made slopes interferes with many geotechnical applications, such as access embankments in bridge projects, extension of road works and earthen dams. The stability of such structures is reliant of two load components: the self-weight and applied loads both at the crest and slope sides. Combining these two load components for a given ground slope with prescribed inclination and water condition is helpful for the design of a foundation in plane strain condition, i.e., strip footing. The overview reported on below shows numerous publications on slope stability dealing with different aspects.

Blong and Dunkerley, 1976, [1]) reported on the difficulty of predicting the triggering of landslides at small depth due to annual and daily rainfall.

Furthermore, slope stability with induced water infiltration can trigger landslides, especially in earth dams. In this framework, Huynh, 2005, [2] performed numerical modelling of landslides by implementing Hill's stability criterion into two finite element codes. This approach has been used to study the behavior of nonlinear boundary problems, such

as for the landslide that occurred on the "Trévoux" hillside after an intense rainfall period in 1983.

Masekanya, 2008, [3], investigated the slope stability in unsaturated soil by incorporating the measurement of suction from laboratory tests. The influence of suction on the slope stability after numerical computations was assessed by experimental results. It was determined that the influence of suction favors an increase in the factor of safety of slope stability.

Allout et al., 2015, [4] performed numerical modelling for studying the behavior and analysis of slope stability of an earthen dam subjected to a simulated earthquake based on that, which occurred in 2003 at Boumerdes (Algeria). The studied case history refers to Taksebt–Tizi Ouzou earth dam. Numerical predictions agreed fairly well with observed displacements for which the stability of the dam was not affected.

Studying the presence of water in slopes by infiltration and induced seepage is very challenging. In fact, different influence factors affect the slope stability. Xuan et al., 2016, [5] investigated a slope failure induced by a rainfall phenomenon. These authors proposed 2D experimental and numerical models by integrating seepage flow to determine the critical slope angle to approximate the threshold of a sudden failure. In fact, different influencing factors affect the slope stability, [6–9].

Ben Khalifa et al., 2018, [10] built a laboratory box model in which a compacted sand slope model was subjected to a uniform vertical stress applied at the crest slope up to failure. The authors compared the experimental results to numerical predictions of the failure load by assuming circular slip surfaces.

Later, Abdi et al., 2019, [11] investigated model tests loaded by a rigid plate resting on unreinforced and reinforced sand slopes by geotextiles. They focused on the determination of the ultimate bearing capacity of a rigid plate subjected to an eccentric load located towards or opposite to the facing slope. The authors highlighted the effect of load inclination on the ultimate bearing capacity of a strip footing that represents a major concern as pointed out by several authors.

For this application, previous research showed that the soil total unit weight (γ) has a limited influence on the failure load of the ground slope, [1–4,6–10,12–15]. In a recent study, Karoui et al., 2020, [7] investigated the stability of a deposited phosphogypsum embankment by finite element method. A plane strain model was proposed to predict the evolution of settlement and horizontal displacement during the operations of stage construction of the phosphogypsum embankment. Mohr–Coulomb constitutive law was adopted during the computations. The stability of phosphogypsum embankment prevailed during construction when the slope angle did not exceed 20°.

Khan et al., 2021, [9] studied the use of Recycled Plastic Pins (RPPs) to reinforce slopes ranging from 25% to 50% constructed with a highly plastic Yazoo clay (HPYC). Three uniform and varied RPPs spacings were investigated by using the finite element Plaxis 2D code. The numerical results indicated that RPPs provide shear resistance for the sloping HPYCS embankment. For instance, by maintaining a uniform spacing between the RPPs, the factor of safety increased to about 1.7 for the 50% slope case.

Husein Malkawi et al., 2022, [13] determined the properties of phosphogypsum stockpiles in Aqaba, Jordan in order to evaluate their stability by utilizing limit equilibrium and finite element methods. They determined that all studied slopes were stable under all static and seismic loading conditions.

The main objective of the present work is the determination of the failure load induced by a rigid plate on a compacted sand slope model. The applicability of such an investigation is wide and should be followed up during the construction phase in terms of the stability of excavations in the presence of surcharge loads located at the upstream side. In particular, for soils of negligible cohesion, it is impossible to test vertical slopes without the retaining systems when the excavation depth exceeds 5 m. For this reason, slope angles between 30° and 35° are expected to provide reliable results.

An existing experimental laboratory model, [10], permitted us to carry out a series of loading tests to record the failure load of the compacted sand slope model.

Then, a parametric study was performed to highlight the influence of the slope angle α and the location of the applied loading at the crest of the compacted sand slope.

A built numerical model including the boundary conditions and the geotechnical parameters of the compacted sand slope was presented. Then, using the 3D Plaxis code, the behavior of the experimental slope model, subjected to a constant rate of vertical displacement, was simulated up to the failure load. Furthermore, this research investigated the prediction of the failure load of tested models in the yield design framework. The numerical and analytical predictions were compared to the experimental results to assess the performed numerical and analytical modelling.

2. Experimental Study

2.1. Materials and Methods

The experimental slope model comprises compacted sand resting on a stratum layer. The geometrical parameters of this scaled 3D test model, shown in Figure 1, are as follows: maximum height = 0.40 m at the crest level; minimum height at the toe level = 0.25 m; total length L = 0.69 m and thickness B = 0.25 m. This laboratory model simulates at full scale an excavation of a 6 m depth with a slope of length equal to 11.2 m and width equal to 10 m. The scale used is 1/40.

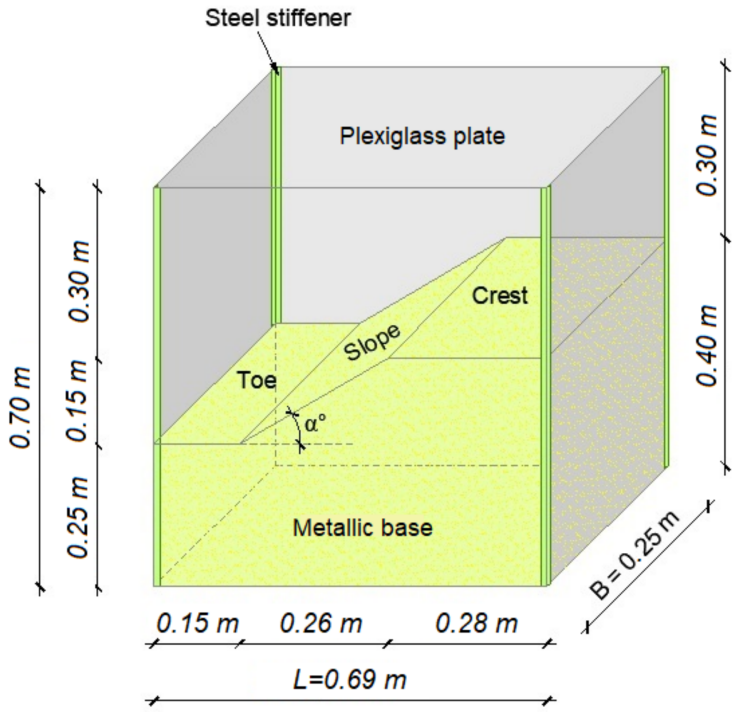

Figure 1. Studied slope model for slope angle equal to 30°.

The experimental study considered two values of the slope angle, α = 30° and 35°. Cohesion less sands have a friction angle that ranges from 28° (loose state) to 38° (dense state). When a slope angle is less than the friction angle of sand, the slope stability holds. Therefore, since in practice, it is much better to excavate at the highest slope angle, the minimum value of the tested slope angle is 30°. In addition, excavating a dense sand layer of an in situ friction angle equal to 38° causes little disturbance to the soil, so that the friction angle is reduced. Hence, the logical maximum slope angle should be approximately 35°, which is the highest value tested in the experiments.

The rigid box comprises 2 × 2 vertical Plexiglas plates of respective areas 0.69 × 0.70 m^2 and 0.70 × 0.25 m^2 (Figure 1). These plates were assembled at the corners by four steel

stiffeners; this set was fixed at the bottom side of a metallic rigid plate of area 0.69 × 0.25 m^2 (Figure 1). As adopted, the geometry, boundary conditions, and loading conditions of the built test model were set as a reference model.

For running the experimental investigation aiming at the determination of the failure load of the slope model shown in Figure 1, a box made up of Plexiglas plates, thickness of 0.03 m, and stiffened by steel corners was used with the following dimensions: height = 0.70 m; length = 0.70 m; and width = 0.25 m (Figure 2). This box model served initially to perform experiments on the sand slope model designed by Ben Khalifa et al., 2018, [10].

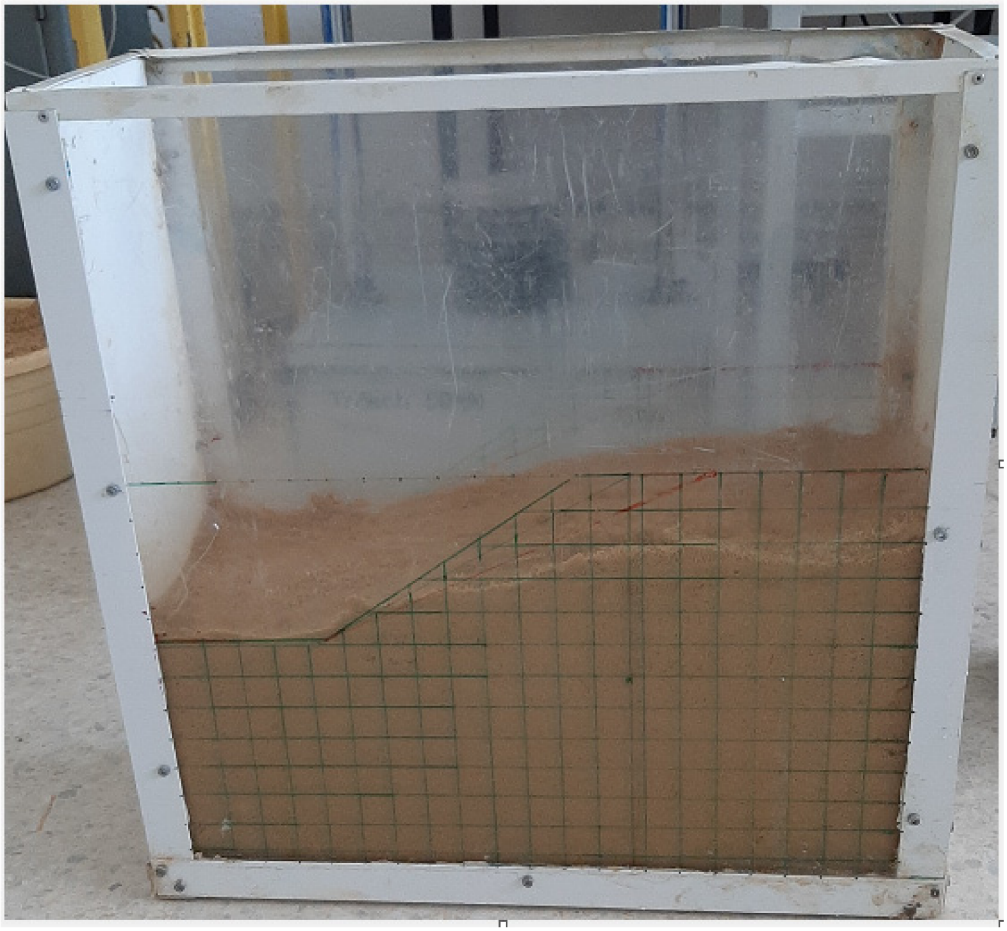

Figure 2. Built Plexiglas box for the scaled test model.

The built slope model resulted from the placement of a homogenized mixed sand, at water content equal to 8%, inside the Plexiglas box by sub-layers each of 0.10 m thickness. Then, the sand sub-layer was gently compacted by hand using a rigid plate of width of 0.06 m and length of 0.24 m. The friction angle of the tested sand equaled 27° and exhibited a weak cohesion of 2 kPa. It is worth noting that these strength parameters are quite different from those of the sand tested in [10]. Table 1 presents the geometry of the built slope models and the configurations of applied loading detailed below.

Table 1. Geometry of tested slope models.

Model Test Identifier (α: Slope Angle)	Rigid Plate (RP)	
	Rigid Plate Area (m^2)	Location at Crest
M1 (30°)	RP1: 0.24 × 0.24	Entire
M2 (30°)	RP2: 0.12 × 0.24	Left
M3 (30°)	RP3: 0.06 × 0.24	Left
M4 (30°)	RP3: 0.06 × 0.24	Center
M5 (30°)	RP3: 0.06 × 0.24	Border
M6 (35°)	RP1: 0.24 × 0.24	Entire
M7 (35°)	RP2: 0.12 × 0.24	Left
M8 (35°)	RP3: 0.06 × 0.24	Left
M9 (35°)	RP3: 0.06 × 0.24	Center
M10 (35°)	RP3: 0.06 × 0.24	Border

2.2. Loading Conditions

The built sand slope model was subjected to an imposed rate of vertical displacement equal to 2 mm/min resulting from a quasi-static compression controlled by the motor drive of a triaxial apparatus. This vertical loading is located at the upper side at the crest of the slope model by means of a rigid steel plate. Figure 3 depicts the locations of a rigid plate (RP) of width b and length B. Three rigid plates (RP1, RP2, and RP3) of different dimensions were used for the applied loading. The performed tests considered three values of the width of the rigid plate: RP1: b = 0.24 m; RP2: b = 0.12 m; and RP3: b = 0.06 m. The thickness of the slope model, in the perpendicular direction of Figure 1, is equal to the length of the rigid plates that equals 0.24 m.

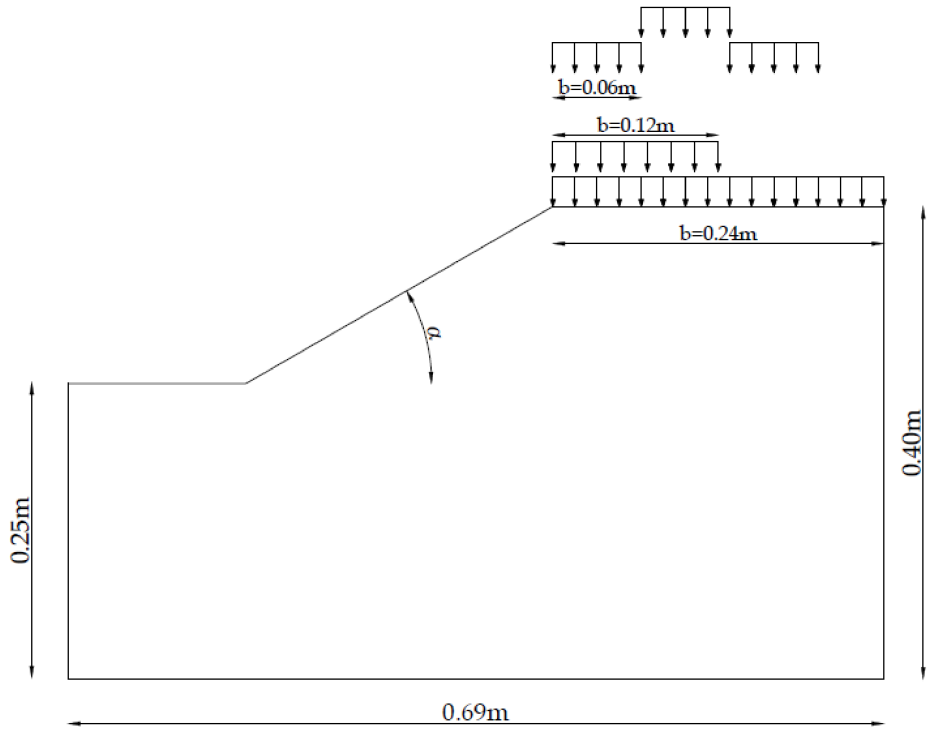

Figure 3. Location of the applied loading at the crest of slope model.

The effect of the unit weight of the compacted sand is negligible with respect to the applied loading by the rigid plate under which the sand slope model fails.

Performed tests. The experimental programme featured ten loading tests that included the variation of the location of the rigid plate with respect to the crest of the slope, the width of the rigid plate and the value of the slope angle. The saturation by water of the compacted sand slope was not part of the carried out experimental investigation.

The evolution of the recorded load for each test model was monitored in parallel to time to failure phase with displayed curves using a GDS Lab system. The recorded load corresponds to the reaction of the slope-tested model against the imposed rate of vertical displacement by means of the rigid plate

2.3. Experimental Results

The load–time curves recorded from the tested scaled models did not almost show peak values of the failure load. Using Equation (1), one can calculate the vertical displacement under the rigid plate placed at the crest side:

$$Uz0 = v \cdot t, \quad (1)$$

where v is the rate of vertical displacement; t is the time. Hence, the determination of the failure load of the tested slope models considered a maximum value of the vertical displacement equal to 3% to 10% of the width of the rigid plate. Using Equation (1), one can determine the vertical displacement at the interface between the rigid plate and the crest level. This vertical displacement U_{z0} was ascertained by readings during the load test from the drawn squared mesh on the Plexiglas border as shown in Figure 4. The side of all the mesh squares is equal to 3 cm.

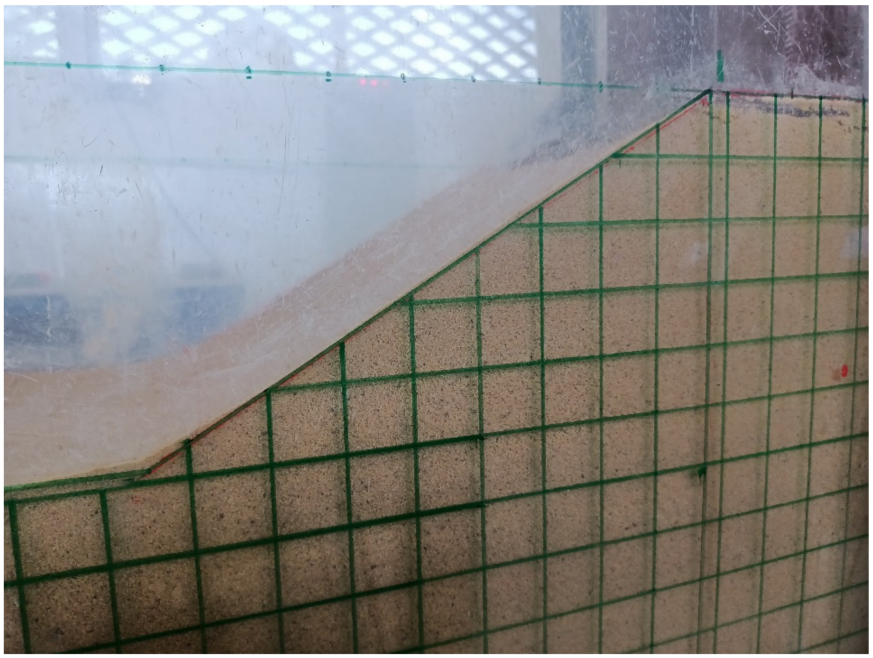

Figure 4. Squared mesh drawn on the Plexiglas plate.

2.3.1. Recorded Failure Loads

Table 2 summarizes the values of the failure load denoted P_{ult} and the corresponding vertical displacement for each tested model as recorded from experiments.

Table 2. Experimental results of the tested slope models.

Model Test Identifier (Slope Angle)	P_{ult} (kN)	U_{z0} (mm)
M1 ($\alpha = 30°$)	10.0	9.2
M2 ($\alpha = 30°$)	1.57	8.5
M3 ($\alpha = 30°$)	0.50	6.0
M4 ($\alpha = 30°$)	0.85	4.5
M5 ($\alpha = 30°$)	0.86	4.5
M6 ($\alpha = 35°$)	2.80	8.0
M7 ($\alpha = 35°$)	1.87	8.0
M8 ($\alpha = 35°$)	10.0	9.2
M9 ($\alpha = 35°$)	1.57	8.5
M10 ($\alpha = 35°$)	0.50	6.0

From Tables 1 and 2, comparing between recorded failure loads of test models M1, M2 and M3, it is clear that the smaller the width of the rigid plate, the more the failure load decreases significantly (from 10 kN to about 1.5 kN). In other words, the closer the concentration of the applied load is to the facing slope, the lower the resistance exhibited by the sand slope model.

Figure 5 shows the recorded load–time curves of the models M3, M4 and M5 tested with a rigid plate of width of 0.06 m placed in three locations. Comparing models M3 and M4, it is obvious that the failure load increased (from 0.5 kN to 0.85 kN) when the applied load moved away from the slope side. In turn, since equal failure applies for test models M4 and M5, it appears the failure laod is no more affected when the rigid plate moves from the center to the border of the slope model of angle $\alpha = 30°$.

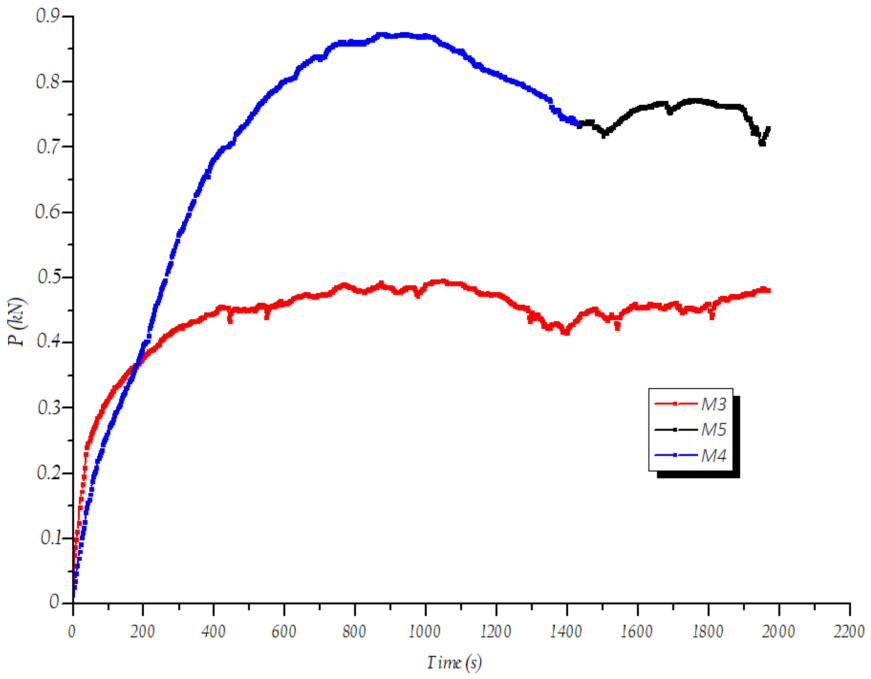

Figure 5. Recorded load–time curves for tested models M3, M4 and M5.

Figure 6 shows the recorded load–time curves of models M6, M7 and M8 tested with the same applied load condition (Figure 3) for models M3, M4 and M5. Recorded failure loads of models M6, M7 and M8 confirmed that when the slope angle $\alpha = 35°$, the

influence of the location of applied load vanishes between the center and the border of the slope model.

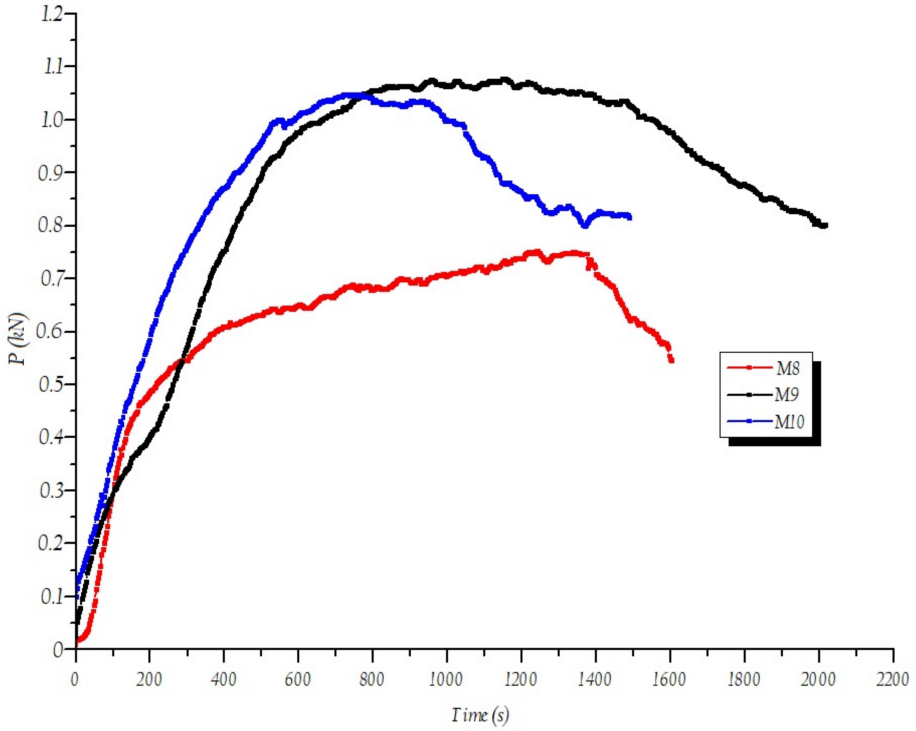

Figure 6. Recorded load–time curves for tested models M8, M9 and M10.

Figure 7 clearly illustrates the influence of the slope angle on the recorded failure loads for test models M1 and M6. At the time of the pre-failure of test model M1, the same corresponding vertical displacement from Equation (1), there is a significant decrease in the failure load (from 10 kN to 2.8 kN) that is attributed to the increase in the slope angle from 30° (model M1) to 35° (model M6).

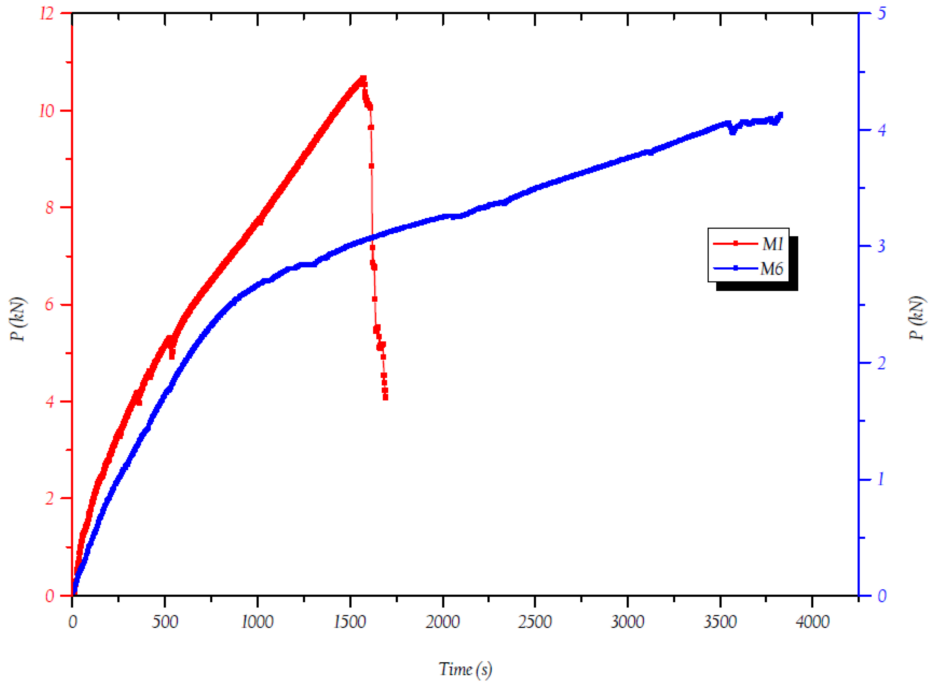

Figure 7. Recorded load–time curves for tested models M1 and M6.

2.3.2. Observed Failure Surfaces—Discussion

Figure 8 shows the views of the facing slope when the failure load is attained for the tested slope models M3, M4 and M5. The difference between those models is the loaction of the rigid plate of width of 0.06 m by which the vertical displacement is applied at the crest side in three locations (Table 1):

(**a**) RP3 adjacent to slope (**b**) RP3 at 0.06 m to slope (**c**) RP3 at 0.12 m to slope

Figure 8. Views from the slope side showing the intercepts of failure surfaces observed for models M3, M4 and M5 loaded with different locations of rigid plate RP3.

-A-: adjacent to the slope, tested for model M3;
-B-: distanced 0.06 m from the slope, tested for model M4;
-C-: distanced 0.12 m from the slope, tested for model M5.

From Figure 8, it is clear that the further back the rigid plate is from the slope side, the greater the depth from which the failure surface emerges at the facing slope from the crest level. The respective recorded failure loads of models M3, M4 and M5 increase when the location of the rigid plates recedes from the facing slope. This is confirmed by a greater length of the failure surface that is proportional to the sand resistance. The load increases because it balances a higher soil resistance.

Figures 9–11 illustrate the localization of the observed failure surfaces from the lateral side of the sand slope for models M3, M4 and M5, respectively. These failure surfaces are not circular in shape; instead, their shape is closer to the log–spiral curve. Validation of the observed failure is detailed in Section 3. Furthermore, the starting point of the observed failure surface is located on the slope side. The logical explanation of this observation is the absence of confinement on the stress-free facing slope on which the failure easily develops. This is contrary to the opposite side where the presence of the vertical Plexiglas plate prevents horizontal displacement; thus, the occurrence of failure is rather unexpected.

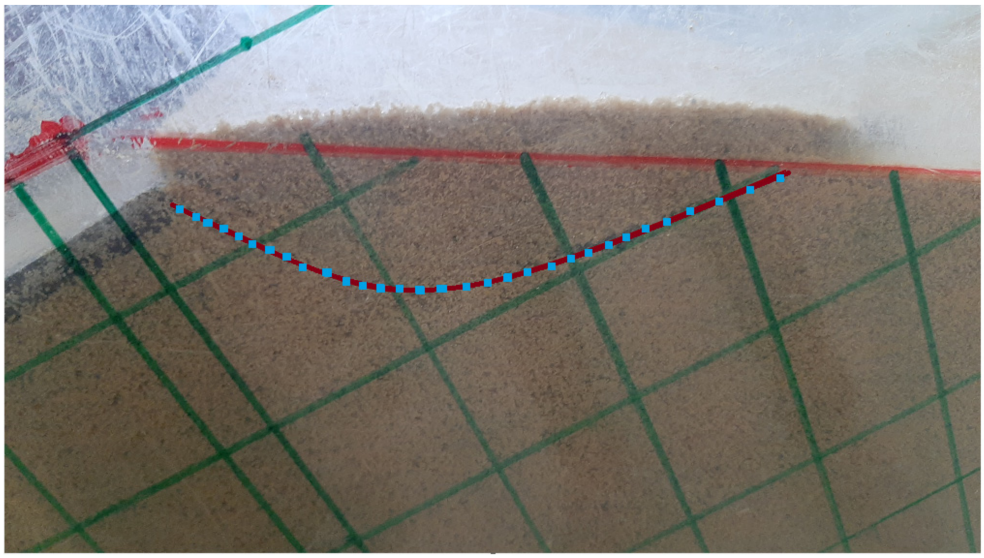

Figure 9. Observed failure surface from the lateral Plexiglas side of the tested model M3.

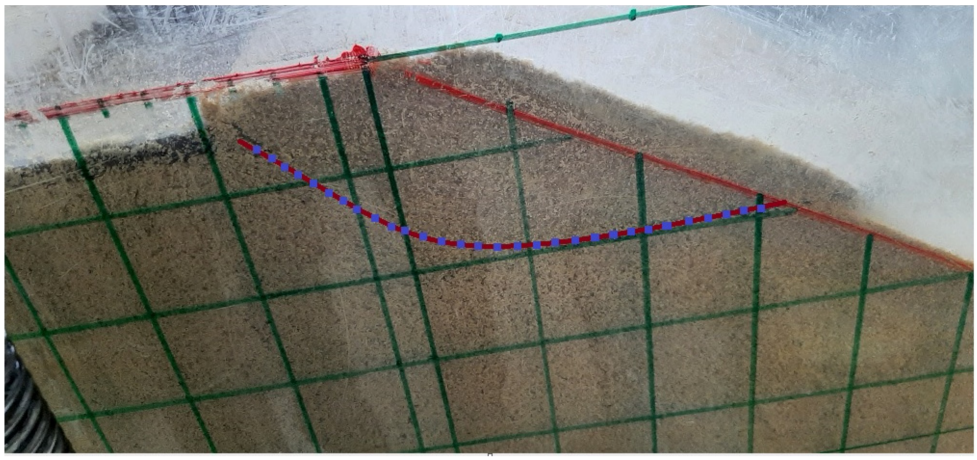

Figure 10. Observed failure surface from the lateral Plexiglas side of the tested model M4.

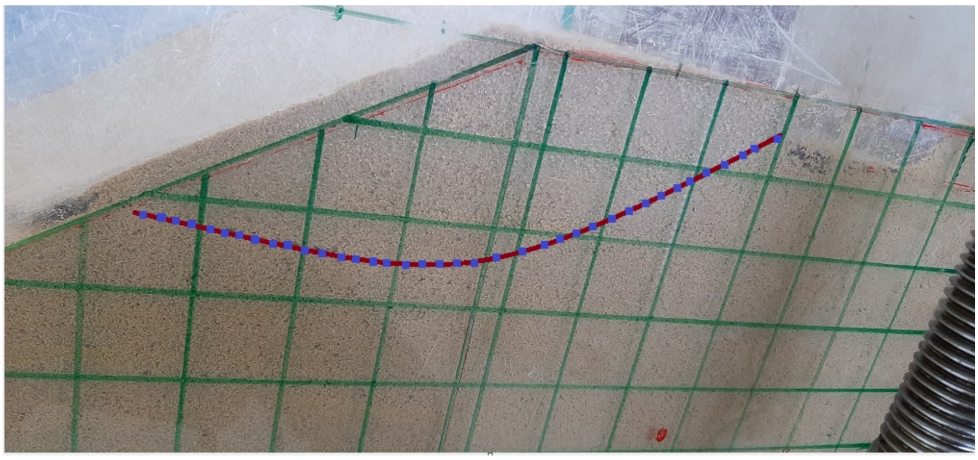

Figure 11. Observed failure surface from the lateral Plexiglas side of the tested model M5.

3. Numerical Study

3.1. The Numerical Model: An Overview

Standard boundary conditions apply for the box model shown in Figure 12, i.e., horizontal displacements are zero along the vertical Plexiglas border, and displacement components are zero at the base of the numerical model. The remaining border of the ground slope model is free of stress, excepting the location of the rigid plate (at crest level) where a uniform rate of vertical displacement is applied.

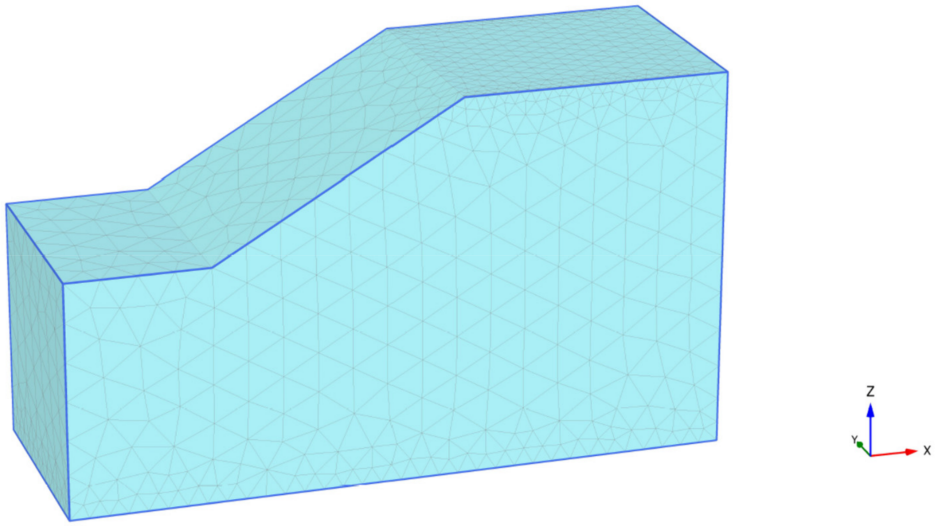

Figure 12. Mesh and boundary conditions of the 3D Plaxis model ($\alpha = 30°$).

The numerical model also considers the resistance reduction factor (R_{inter}) that controls the roughness between the rigid plate and the crest of the sand slope. The present study considered the value $R_{inter} = 0.67$.

The numerical model considered the weight of the rigid plate. Furthermore, along the vertical sides of the box model, contact areas with the compacted sand were modelled as frictional interfaces with a resistance reduction factor $R_{inter} = 0.5$.

3.2. Built Numerical Model

Numerical computations were conducted for the 3D slope model shown in Figure 1 and various loading configurations displayed in Figure 3. The three-dimensional finite-element type was selected with the option of an automatically generated mesh by Plaxis 3D code. This mesh counts 29.146 nodes and 17.581 3D finite elements of 10 nodes of 70.324 stress-points.

Figure 12 shows the generated mesh of the 3D numerical model for the ground slope of angle equal to 30°, referenced as "case study No.1"; the slope angle equal to 35° refers to "case study No.2".

Two constitutive models describe the behavior of compacted sand: the Mohr–Coulomb (MC) model and the hardening soil model (HSM). Table 3 summarizes the adopted geotechnical parameters of these constitutive models. MC constitutive law remains the current reference to describe the soil behavior by using few parameters, easily determined from routine laboratory tests.

Table 3. Geotechnical parameters of the compacted sand: Mohr–Coulomb (MC) and the hardening soil model (HSM) constitutive models.

Parameters	HSM	MC
γ ·(kN/m^3)	**18**	**18**
E_{50}^{ref}·(MPa)	8	*
E_{oed}^{ref}·(MPa)	8	*
E_{ur}^{ref}·(MPa)	24	*
ν_{ur}	0.2	*
E·(MPa)	*	8
K_0^{nc}	0.546	*
m	0.5	*
C·(kPa)	2	2
ν	*	0.33
φ·(°)	27	27

The HSM necessitates further parameters to describe, in a more realistic manner, the nonlinear soil behavior and the hardening effect missed by the MC model. Appendix A, presents the method of determining the parameters of HSM.

Adoption of the HSM proved to be suitable for describing loose sands susceptible to liquefaction, [8]. Moreover, dilatancy is a specific behavior observed for sands that occurs in pre-failure phase. Acharyya and Dey, 2018, [16] reported on the importance of the dilatancy on the evolution of failure mechanism of horizontal ground loaded by a rigid plate.

3.3. Validation of Numerical Results by the Experimental Ones

Table 4 summarizes the predicted values of the ultimate (e.g., failure) load, denoted P_{ult}, for each tested model by the MC and HSM constitutive laws adopted for the compacted sand.

Table 4. Numerical predictions of the simulated slope models.

Model Test Identifier (Slope Angle)	Constitutive Laws			
	Mohr Coulomb (MC)		Hardening Soil Model (HSM)	
	P_{ult} (kN)	U_{z0} (mm)	P_{ult} (kN)	U_{z0} (mm)
M1 (α = 30°)	9.35	6.5	4.00	9.0
M2 (α = 30°)	1.50	8.5	1.33	8.5
M3 (α = 30°)	0.51	4.0	0.41	6.0
M4 (α = 30°)	0.83	4.5	0.55	4.5
M5 (α = 30°)	0.94	4.5	0.61	4.5
M6 (α = 35°)	3.70	8.0	2.70	8.0
M7 (α = 35°)	1.87	8.0	1.66	8.0
M8 (α = 35°)	0.74	8.0	0.61	8.0
M9 (α = 35°)	0.90	4.5	0.64	4.5
M10 (α = 35°)	1.04	6.0	0.75	6.0

3.3.1. Case Study No.1: α = 30°

Figure 13 shows that the MC predictions for model M1 fit well with the experimental behavior. The adopted value of the failure load is 10 kN based on a maximum vertical

displacement at crest level equal to 9 mm. By contrast, the HSM prediction is far from the recorded experimental value. The predicted evolution of the load–displacement curve using the HSM does not attain a peak value up to a vertical displacement approximating 10 mm.

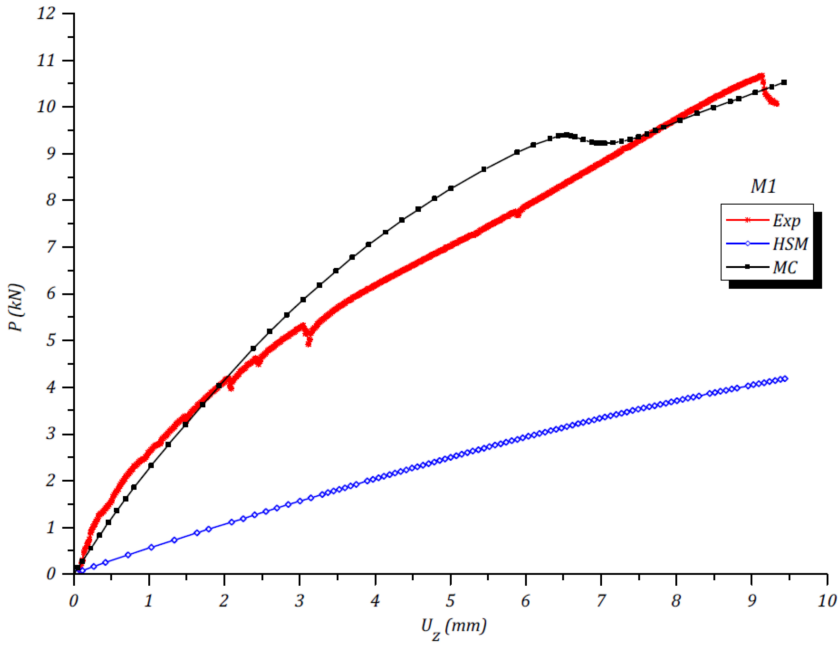

Figure 13. Evolution of the reaction force versus vertical displacement (M1).

As seen in Figure 14, model M2 indicates that the experimental failure load is in between the numerical predictions. However, the HSM provides a better fit with the observed behavior.

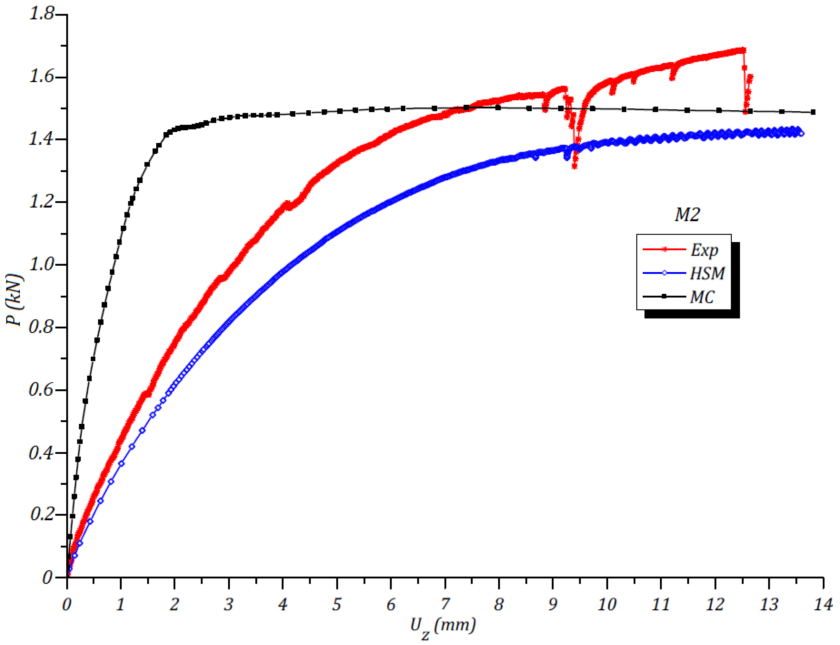

Figure 14. Evolution of the reaction force versus vertical displacement (M2).

Figure 15 shows that the overall observed behavior of the slope model M3 and the recorded failure load match better with the predictions by the MC model.

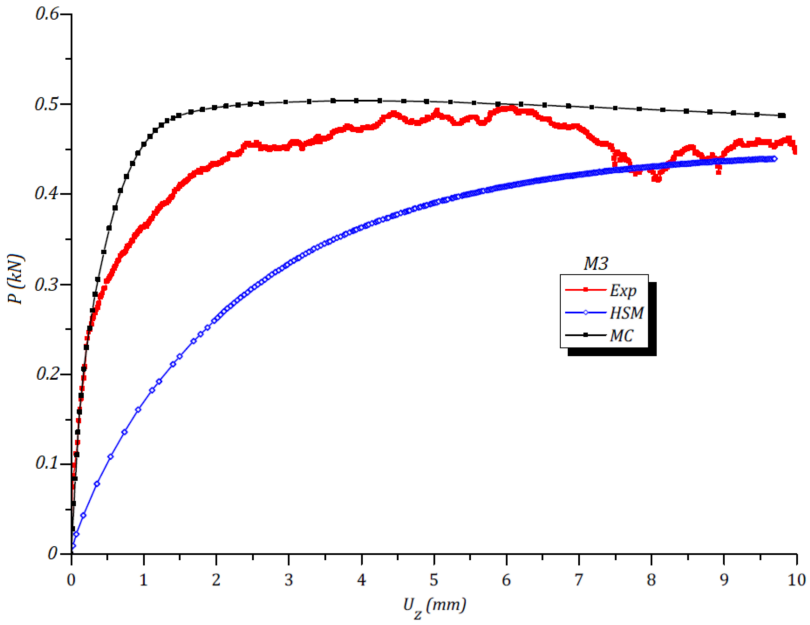

Figure 15. Evolution of the reaction force versus vertical displacement (M3).

Furthermore, the HSM predictions for models M1, M2 and M3 underestimate the failure load when the vertical displacement is less than 7 mm. This underestimation is very marked, as observed for model M1 (Figure 13).

From Figures 15–17, the comparison between the load–displacement curves for the slope model of angle $\alpha = 30°$ shows that the failure load increases from 0.5 kN to 0.86 kN when rigid plate RP3 of width b = 0.06 m is moved away from the facing slope. This obvious result confirms that the slope stability improves when the applied load moves away from the slope side.

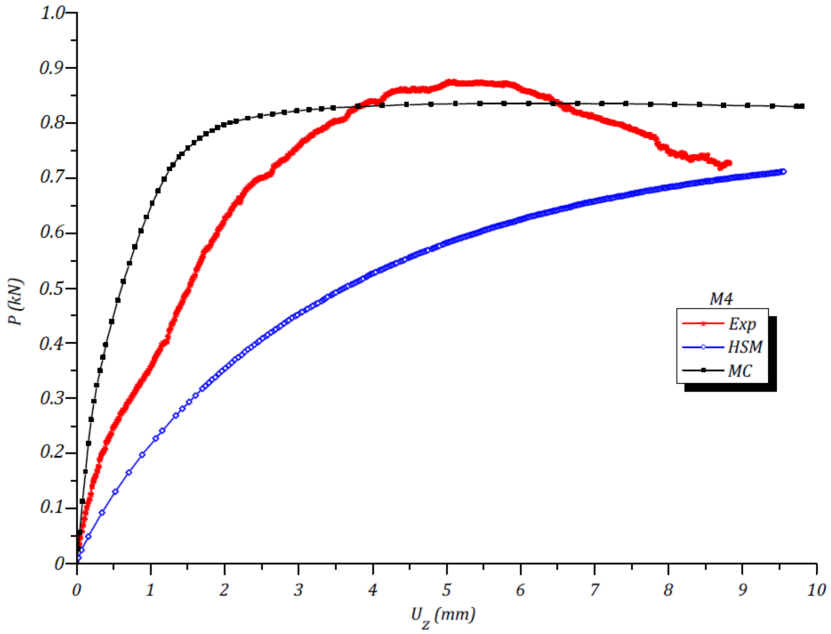

Figure 16. Evolution of the reaction force versus vertical displacement (M4).

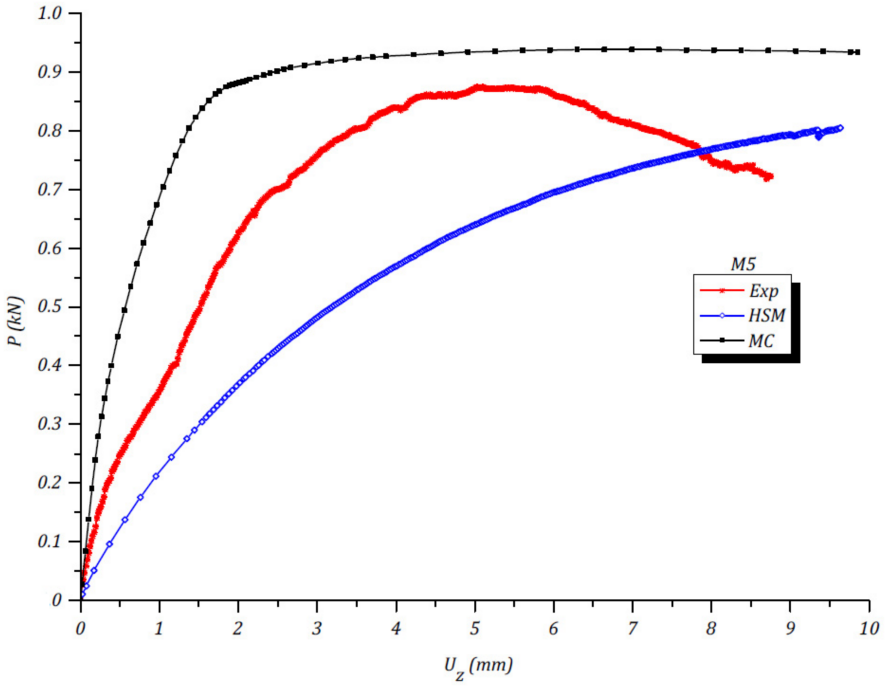

Figure 17. Evolution of the reaction force versus vertical displacement (M5).

3.3.2. Case study No.2: $\alpha = 35°$

From Figures 18–20, the comparison between models M6, M7 and M8 shows that the more the location of applied loading moves towards the crest slope, the more the failure load decreases.

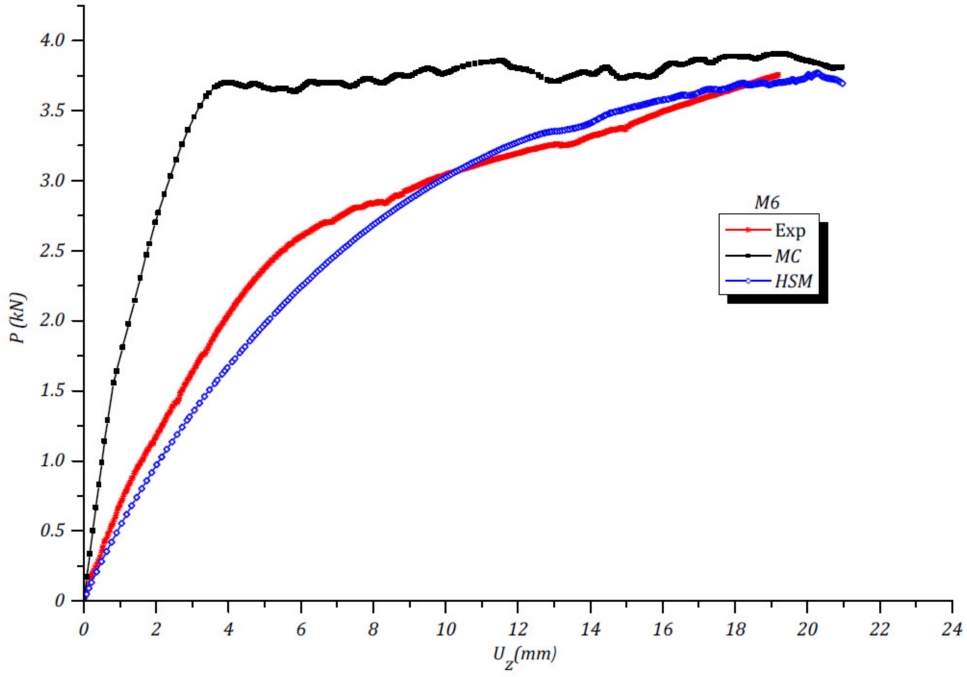

Figure 18. Evolution of the reaction force versus vertical displacement (M6).

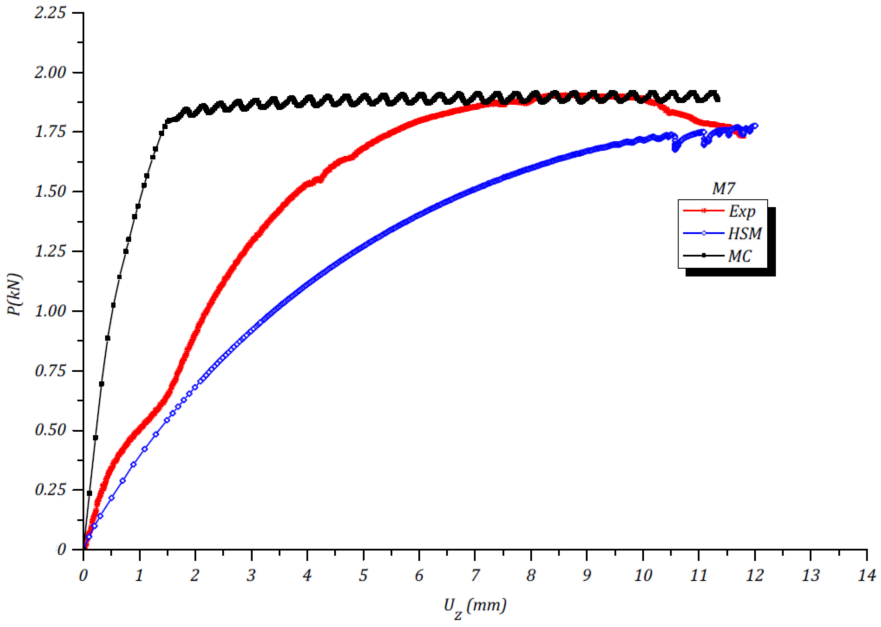

Figure 19. Evolution of the reaction force versus vertical displacement (M7).

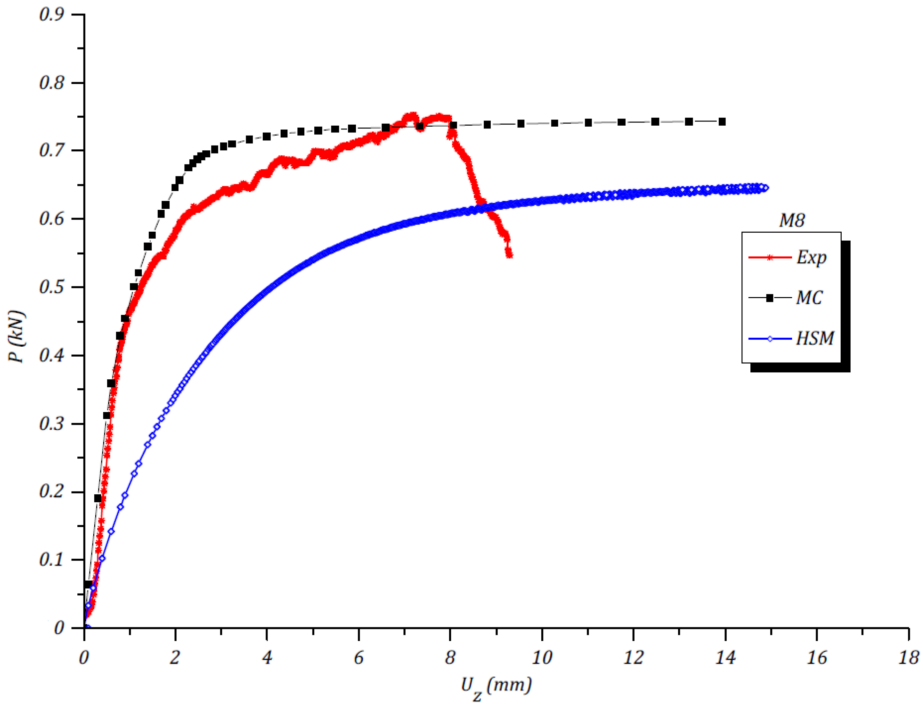

Figure 20. Evolution of the reaction force versus vertical displacement (M8).

In turn, the HSM predictions of the failure load are in much better agreement with the experimental values recorded with test models M6 and M7. One can conclude that when the angle of compacted sand slope model increases from 30° to 35°, the HSM predicts a realistic decrease in failure load compared to the prediction by Mohr–Coulomb model.

From Figures 20–22, it is clear that the global experimental behavior fairly matches with predictions by the MC constitutive law both for the magnitudes of failure load and vertical displacement recorded under rigid plate RP3 at the crest side of the tested slope models M8, M9 and M10.

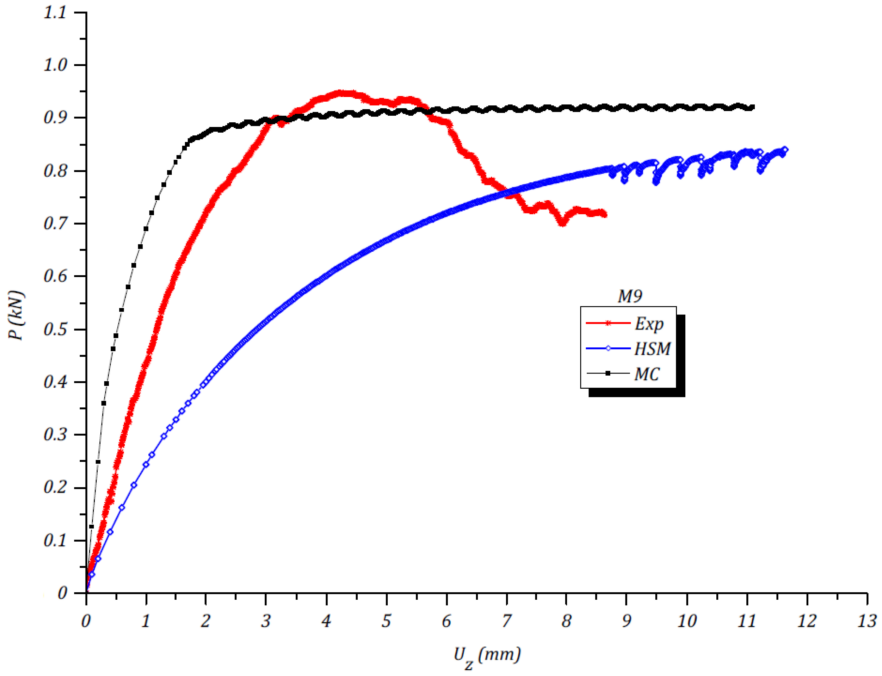

Figure 21. Evolution of the reaction force versus vertical displacement (M9).

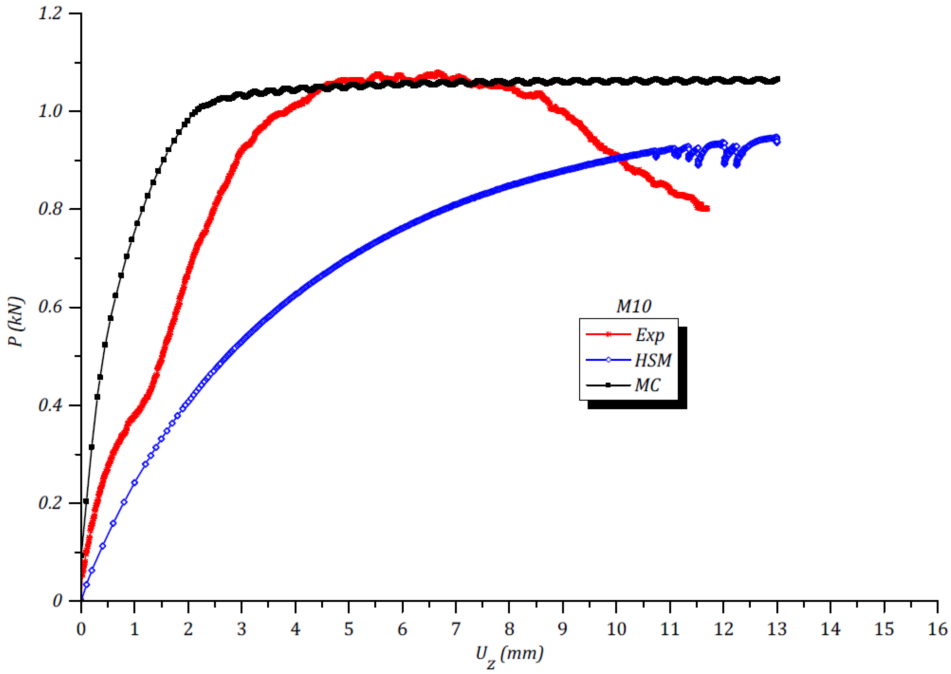

Figure 22. Evolution of the reaction force versus vertical displacement (M10).

Moreover, the HSM overestimates the recorded vertical displacement and underestimates the magnitude of failure load by 19%, 27% and 29% when the applied loading moves away from the slope side, respectively.

As shown in Figure 23, the value of the vertical displacement under the rigid plate tends toward a maximum value of 16 mm, and the observed failure surface of this model (M9) fits with a log–spiral failure curve.

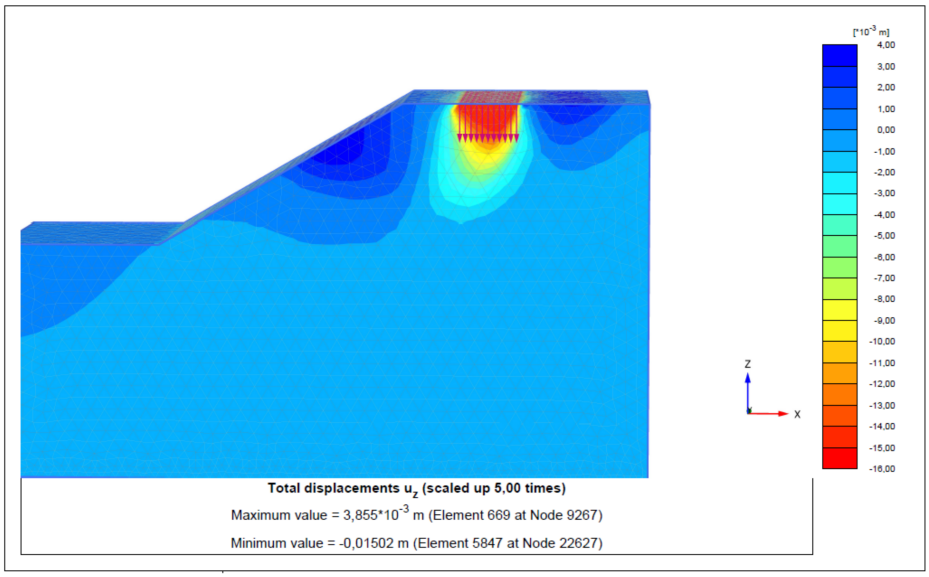

Figure 23. Total displacement u_z and failure surface for the numerical model (M9).

Table 5 summarizes the relative differences between the experimental values of the failure load and its predictions by the Mohr–Coulomb and hardening soil models. Absolute values of these relative differences indicate that the MC model predicts the experimental values of the failure load much better (relative difference lower than 10%) for all models except model M6. For the latter, the HSM predicted the failure load much better, with a weak relative difference.

Table 5. Relative differences between the recorded failure loads and numerical predictions by the Mohr–Coulomb and hardening soil models.

P_{ult} (kN) Experimental	Relative Differences (%)			
	P_{ult} (kN) MC	P_{ult} (kN) HSM	Experimental—MC	Experimental—HSM
10.0 (M1)	9.35	4.0	10.9	61.9
1.57 (M2)	1.50	1.33	4.5	15.3
0.50 (M3)	0.51	0.41	2.0	18.0
0.85 (M4)	0.83	0.55	2.5	35.3
0.86 (M5)	0.94	0.61	8.1	29.1
2.80 (M6)	3.70	2.70	32.1	3.6
1.87 (M7)	1.87	1.66	0.0	15.5
10.0 (M8)	0.74	0.61	1.3	18.7
1.57 (M9)	0.90	0.64	5.3	34.7
0.50 (M10)	1.04	0.75	2.8	29.9

3.4. Validation of the Log–Spiral Curve of Observed Failure Surfaces

Referring to [17,18], in the framework of the yield design theory (commonly called limit analysis), the ultimate load can be associated to failure mechanisms inducing discontinuities of velocities on assumed failure surfaces described by the log–spiral curve defined by Equation (2):

$$r = r_0 \exp(\delta \, tg\varphi). \quad (2)$$

Figure 24 shows the drawn log–spiral curve characterized by the rotation about the center Ω from the initial radius r_0 = ΩA to the current radius r = ΩZ located at angle

δ. The main characteristic is the following: along this curve, at any point Z, the formed angle between the tangent to the curve and the perpendicular to the current radius vector (ΩZ) equals the friction angle φ of the material. As a result, the final radius of the drawn log–spiral curve results from the rotation, over angle θ, is $r_f = \Omega B = r_0 \exp(\theta \, tg\varphi)$.

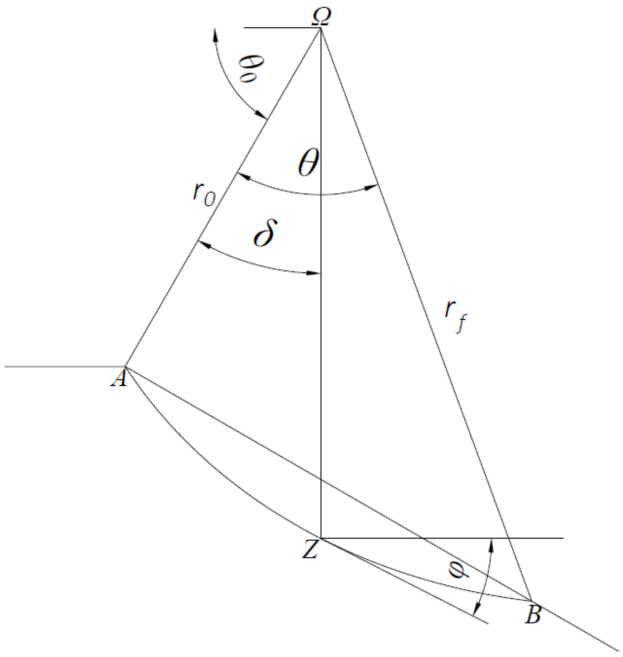

Figure 24. Geometrical parameters of the log–spiral curve drawn from the observed failure surface.

Regarding the observed failure surfaces for models M3, M4 and M5, Table 6 summarizes the geometrical parameters of the best-fitted log–spiral curves. Equations of these curves consider the starting point of observed failure surfaces close to the rigid plate, and the final point is located on the slope side. The approximated location of rotation center Ω fulfills the condition ΩB > ΩA.

Table 6. Analytical prediction of the failure load, using the log–spiral failure surface, for models M3, M4 and M5.

Test Model	Initial Radius r_0 (m)	Vertex Angle θ (°)	Tangent Angle (°)	Final Radius r_1 (cm)	Angle θ_0 (°)	Failure Load (kN/lm)
M3	0.118	50	27	17.4	60	4.15
M4	0.140	47	27	21.2	70	3.07
M5	0.250	47	27	38.0	75	4.15

Figure 25 compares the theoretical log–spiral curve obtained by Equation (2) and the observed failure surface for model M5 as reproduced from the drawn dashed curve in Figure 11. The good agreement between the two curves confirms that the assumed circular surface for frictional material does not prevail. Furthermore, the current attributed term in soil mechanics "sliding surface" is not meaningful since the discontinuity of velocity along the tangent of the log–spiral forms makes the theoretical angle equal to the frictional angle of the soil as clearly shown in Figure 25.

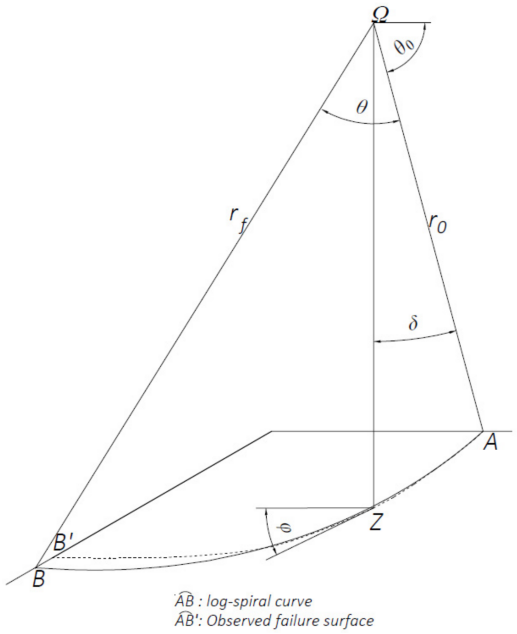

Figure 25. Validation of the analytical log–spiral curve by the observed failure surface for model M5.

3.5. Analytical Prediction of the Failure Load of Tested Models M3, M4 and M5

Adopting the kinematic approach of the yield design theory (Salençon, 1990), the log–spiral failure surface corresponds to a surface of discontinuity of velocity that results from the rotation of the slope portion formed between the crest, the slope facing and the failure surface, and is subject to the rotation velocity ω around the center Ω.

Therefore, along the tangent to the log–spiral curve (AB), the discontinuity of velocity between the rotating slope portion and the rest of the ground slope is described in Equation (3):

$$\underline{V} = \omega \, r \, \underline{e}_t, \tag{3}$$

where $\underline{e}_t$ denotes the tangent unit vector to the log–spiral curve.

Equation (4) traduces the compatibility condition for the kinematic admissible constructed velocity field obtained by Equation (3):

$$U_{z0} = V_0 \cos\theta_0. \tag{4}$$

U_{z0} is the downward velocity displacement of the rigid plate ensuring the applied loading at the crest slope. From Equation (3), the velocity displacement corresponding to the initial radius r_0 is

$$V_0 = \omega . r_0. \tag{5}$$

Then, according to the kinematic theorem of YDT, one obtains an upper bound solution of the failure load from the condition traducing that the work of external forces is bound by the maximum resisting work developed over the surface of discontinuity of velocity (AB). The considered velocity field (movement of rigid block) does not induce deformation within the sand slope for which the gravity is neglected; thus, it comes

$$P_{ult} \leq \frac{C. \cot g\phi}{2. \cos\theta_0} . r_0 \left[e^{2\theta . tg\phi} - 1 \right]. \tag{6}$$

Equation (6) provides the analytical upper-bound solution of the exact failure load value denoted by P_{ult}. In plane strain condition, the predicted value of this failure load from Equation (6) is assessed per lineal meter (kN/lm).

Validation of the analytical upper-bound predictions of the failure load summarized in Table 6 (e.g., plane strain condition) needs to be multiplied by the geometrical ratio (1/4)

between the width of the rigid plate B = 0.25 m (Figure 1) and the lineal meter. As such, one can compare the experimental and numerical values of the failure loads displayed in Tables 2 and 4 and the predicted values in Table 7.

Table 7. Comparison between the recorded failure load of test models M3, M4 and M5 and the numerical and analytical predictions.

Test Models	Failure Loads (kN)		
	Analytical	Experimental	Numerical
M3	1.04	0.50	0.51
M4	0.77	0.85	0.83
M5	1.04	0.86	0.94

Table 7 summarizes the analytical predicted failure loads for models M3, M4 and M5, and the experimental and numerical values corresponding to the Mohr–Coulomb models since it complies with Mohr–Coulomb strength criterion adopted in the YDT framework.

Comparison of the obtained results for the M3 and M5 models, it appears logical that the upper-bound value of failure load is higher than the experimental and numerical results. However, the analytical prediction of failure load is closer to the numerical prediction. Meanwhile, for model M3, there is a significant difference (approximately 100%) in the analytical prediction compared to the experimental value and numerical prediction. This result may justify the fact that the considered log–spiral curve does not optimize, at best, the upper-bound solution of the failure load. Regarding model M4, the relative differences between the predicted values (numerical and analytical) and the recorded experimental values are not significant; thus, they provide a good estimate of the exact failure load. Hence, one can deduce that the numerical model and the analytical plane strain model are comparable.

3.6. General Comments

For the simulated loading at an imposed rate of vertical displacement, neither the MC nor the HSM constitutive laws can simulate prediction of the decrease in failure load after the peak value, as observed from experiments.

Synthesis of the obtained results shows that the predictions by the HSM fairly agree with the observed behavior of the test models M2–M7 for which the location of applied loading is the same as using rigid plate RP2.

The analytical plane strain model adopting the log–spiral failure surface allowed us to highlight any unsuitable assumptions of circular failure surface in soil mechanics for frictional materials. Importantly, the predicted analytical solution using the rotational failure mechanism proved to be in fair agreement either with the numerical result or with the experimental result.

4. Conclusions

This study determined the failure load of a slope model made up of a compacted sand. The applicability of such an investigation is wide and should be followed up, during the construction phase, in terms of the stability of excavations in the presence of surcharge loads.

An experimental investigation in the laboratory involved the preparation of a slope model, and then loading tests were conducted using an imposed rate of vertical displacement at the crest side. Two angles of the slope models, $\alpha = 30^\circ$ and 35°, and various locations of the applied loading were analyzed for ten slope models. Then, the slope test models were simulated by performing a 3D numerical study using Plaxis code and adopting the Mohr–Coulomb and hardening soil constitutive laws for the compacted sand. The main outcomes of the experimental, numerical and analytical investigations are sum-

marized hereafter. Experimental and numerical results confirmed that the failure load decreases when the angle of the slope model increases from 30° to 35°.

For a given slope angle, the closer the applied loading to the slope side, the smaller the failure load.

Predicted values of the failure load by the Mohr–Coulomb constitutive law fit better with measurements for the majority of tested slope models with a relative difference of less than 11%. On the other hand, only one prediction by the HSM proved to be satisfactory (relative difference equals 3.5%) for a slope test model with an angle of 35°. However, the globally observed behavior (load–displacement curves) of the tested slope models proved to be better described either by the Mohr–Coulomb constitutive law or by the hardening soil model depending on the value of the angle of slope model and the location of applied loading. Considering the framework of the YDT and from the experimental results, the log–spiral curve was determined to be the best model in reproducing the observed failure mechanism.

Assuming the Mohr–Coulomb strength criterion, the analytical plane strain condition can predict a reasonable upper-bound value of the failure load of the sand slope model.

The present paper did not address water drainage within the compacted sand slope, i.e., the absence of a water table. This limitation will be addressed in future work.

Author Contributions: Conceptualization, S.D.; Software, H.K.; Validation, W.F.; Investigation, S.D. and M.B.; Resources, M.D., T.N. and M.E.M.; Writing—original draft, M.B. All authors have read and agreed to the published version of the manuscript.

Funding: This research received no external funding.

Institutional Review Board Statement: Not applicable.

Informed Consent Statement: Not applicable.

Conflicts of Interest: The authors declare no conflict of interest.

Notations

α	slope angle
B (b)	length (width) of rigid plate
HSM	hardening soil model
M	model
MC	Mohr–Coulomb
P_{ult}	failure load
R_{inter}	resistance reduction factor
RP	rigid plate
U_{z0}	vertical displacement at the crest slope
YDT	yield design theory

Appendix A

Appendix: Hardening soil model parameters, in brief

The elastoplastic non-linear isotropic strain hardening model, or the well-known HSM, was suggested to reproduce the observed macroscopic phenomena for grounds [19]:

- Densification, decrease in the volume owed to the plastic deformations (distortions);
- Increase in stiffness with depth;
- Stress–strain history taking account of pre-consolidation effect;
- Dilatancy (resp. contractancy) increase (resp. decrease) in volume.

Contrarily to other models such as the Modified Cam Clay, the amplitude of deformations (distortions) of the soil needed the incorporation of three stiffness parameters: the rigidity of triaxial loading (E_{50}), the rigidity of triaxial unloading–reloading (E_{ur}), and the œdometer modulus (E_{oed}).

Figure A1 displays the stiffness moduli considered by the HSM in the deviator–axial strain plan as usually recorded during shear triaxial test. In this figure, E_0 denotes the tangent stiffness modulus and q_f denotes the failure deviatoric stress.

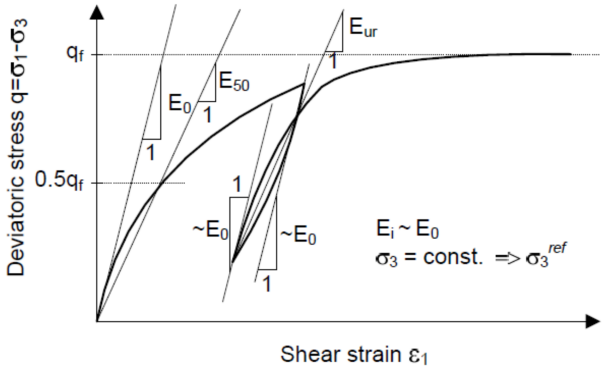

Figure A1. Stiffness moduli adopted by the HSM from typical stress–strain curve recorded in the shear phase of triaxial test.

References

1. Blong, R.J.; Dunkerley, D.L. Landslides in the razorback area, New South Wales, Australia. *Geogr. Ann. Ser. A Phys. Geogr.* **1976**, *58*, 139–147. [CrossRef]
2. Huynh, K. Modélisation Des Glissements de Terrain Comme Un Problème de Bifurcation; Université de Grenoble, France. 2015. Available online: https://theses.hal.science/tel-00085919 (accessed on 13 April 2023).
3. Masekanya, J.P. Stabilité Des Pentes Et Saturation Partielle. Etude Expérimentale Et Modélisation Numérique. Ph.D. Thesis, Université Libre de Liège, Liège, Belgium, 2018.
4. Allout, N.; Gueddouda, M.K.; Goual, .I. Modélisation et simulation numérique de la stabilité des pentes dans les barrages en terre durant un séisme—Cas du barrage de Taksebt-Tizi-Ouezzou. In Proceedings of the 13th Arab Structural Engineering Conference, Blida, Algeria, 13–15 November 2015.
5. Xuan, K.D.; Kwansue, J.; Giha, L.; Ram, K.R. A study of rainfall induced slope failures: Implications for various steep slope inclinations. *J. Korean Geo Environ. Soc.* **2016**, *17*, 5–16. [CrossRef]
6. Ijaz, N.; Ye, W.; Rehman, Z.U.; Dai, F.; Ijaz, Z. Numerical study on stability of lignosulphonate-based stabilized surficial layer of unsaturated expansive soil slope considering hydro-mechanical effect. *Transp. Geotech.* **2022**, *32*, 100697. [CrossRef]
7. Karoui, H.; Maazoun, H.; Bouassida, M. Numerical simulation of wet deposited Phosphogypsum embankment resting on dry deposited one. *Arab. J. Geosci.* **2020**, *13*, 817. [CrossRef]
8. Karoui, H.; Bouassida, M. Assessment of observed of behavior of Sidi El Barrak Dam (Tunisia). *Innov. Infrastruct. Solut.* **2016**, *1*, 44. [CrossRef]
9. Khan, M.S.; Nobahar, M.; Ivoke, J. Numerical Investigation of Slope Stabilization Using Recycled Plastic Pins in Yazoo Clay. *Infrastructures* **2021**, *6*, 47–53. [CrossRef]
10. Ben Khalifa, M.; Djelabi, S.; Frikha, W.; Jellali, B. Etudes expérimentale et numérique de la stabilité d'un talus soumis à un chargement statique vertical. In Proceedings of the ISRM 1st International Conference on Advances in Rock Mechanics-TuniRock 2018, Hammamet, Tunisia, 29–31 March 2018; Hamdi, E., Ed.; pp. 1273–1278.
11. Abdi, A.; Abbeche, K.; Athmania, D.; Bouassida, M. Effective Width Rule in the Analysis of Footing on Reinforced Sand Slope. *Stud. Geotech. Mech.* **2019**, *41*, 42–55. [CrossRef]
12. Acharyya, R.; Dey, A. Finite Element Investigation of the Bearing Capacity of Square Footings Resting on Sloping Ground. *INAE Lett.* **2017**, *2*, 97–105. [CrossRef]
13. Husein Malkawi, D.A.; Husein Malkawi, A.I.; Bani-Hani, K.A. Slope Stability Analysis for the Phosphogypsum Stockpiles: A Case Study for the Sustainable Management of the Phosphogypsum Stacks in Aqaba Jordan. *Sustainability* **2022**, *14*, 15763. [CrossRef]
14. Mahmood, K.; Kim, J.M.; Ashraf, M.; Rehman, Z.U. The Effect of Soil Type on Matric Suction and Stability of Unsaturated Slope under Uniform Rainfall. *KSCE J. Civ. Eng. Geotech. Eng.* **2016**, *20*, 1294–1299. [CrossRef]
15. Rahardjo, H.; Ong, T.H.; Rezaur, R.B.; Leong, E.C. Factors Controlling Instability of Homogeneous soils slopes under Rainfall. *J. Geotech. Geoenviron. Eng.* **2007**, *133*, 1532–1543. [CrossRef]
16. Acharyya, R.; Dey, A. Importance of Dilatancy on the Evolution of Failure Mechanism of a Strip Footing Resting on Horizontal Ground. *INAE Lett.* **2018**, *3*, 131–142. [CrossRef]
17. Salençon, J. An Introduction to the yield design theory and its applications to soil mechanics. *Europ. J. Mech. A/Solids* **1991**, *9*, 477–500.

18. Salençon, J. *Calcul à la Rupture Et Analyse Limite*; Editions Presses de L'Ecole Nationale Des Ponts Et Chaussées: Paris, France, 1983.
19. Schanz, T.; Vermeer, P.A. Special issue on pre-failure deformation behaviour of geomaterials. *Géotechnique* **1998**, *48*, 383–387.